Ultrafast electron-electron scattering and energy exchanges in noble-metal nanoparticles

C. Voisin,* D. Christofilos,† P. A. Loukakos, N. Del Fatti, and F. Vallée

*Centre de Physique Moléculaire Optique et Hertzienne CNRS and Université Bordeaux I, 351 cours de la Libération,
33405 Talence, France*

J. Lermé, M. Gaudry, E. Cottancin, M. Pellarin, and M. Broyer

*Laboratoire de Spectrométrie Ionique et Moléculaire CNRS and Université Lyon I, 43 Bd. du 11 Novembre 1918,
69622 Villeurbanne, France*

The conduction electron energy exchanges are investigated in gold and silver nanoparticles with average size ranging from 2 to 26 nm, embedded in different matrices. The experimental studies were performed by following the internal thermalization dynamics of photoexcited nonequilibrium electrons with a femtosecond pump-probe technique. The probe wavelength dependent measurements are in qualitative agreement with the results of a theoretical model based on bulk metal electron kinetics and band-structure modeling. In both metals, the measured electron thermalization times are close to the bulk ones for nanoparticles larger than 10 nm and sharply decrease for smaller ones. The results are independent of the nanoparticle environment and synthesis technique showing that the observed size behavior reflects an increase of the efficiency of the electron-electron energy exchanges in small nanoparticles. It is in agreement with a simple model based on a bulk metal approach of the electron kinetics modified to introduce surface effects. The observed increase of the electron-electron interaction with size reduction is ascribed to reduction of the screening of the Coulomb interaction by the conduction and core electrons close to the nanoparticle surface.

I. INTRODUCTION

The static and dynamic properties of clusters and their evolution with size from quasisolid to quasimolecular behaviors have been an intense field of researches during the last decades. Understanding the physical origin of the new properties of nanoobjects here is of central interest. It is motivated by both fundamental and technological aspects, nanostructured systems being an important class of new materials for applications. In this context, the interaction processes of the elementary excitations inside a cluster and their coupling with the environment (surrounding matrix, adsorbed molecules, other nanoparticles, . . .) are key parameters. However, they are difficult to address with conventional experimental techniques. Time-resolved optical techniques have here emerged as powerful tools for directly studying electron interaction mechanisms in nanomaterials.[1–4] Though many investigations have been performed in nanostructured semiconductors,[1] these techniques have been only recently applied to metal nanoparticles.[2–14] Information have thus been obtained on electron-surface scattering,[13,14] and on electron-phonon,[8–13] and electron-matrix[15–17] energy exchanges. The impact of confinement on electron-electron scattering and on the correlated energy exchanges has only recently been addressed in silver nanoparticles, yielding evidence for increase of the electron-electron interactions for sizes smaller than 10 nm.[18] In this paper we are discussing in more details these first measurements, in particular, their optical wavelength dependence, and extending them to gold clusters embedded in different environments. The results in both metals are interpreted in term of surface induced reduction of the screening of the Coulombic interactions.

Electron-electron interactions and the correlated internal thermalization kinetics have been investigated in bulk noble metals using different time-resolved techniques: two-photon photoemission, transient optical property modulation, surface-plasmon polariton kinetics, and picosecond ultrasonics.[19] All indicate a slow establishment of the electron temperature on a few hundred femtosecond time scale. Investigations performed in nanoparticles use an extension of the optical property modulation technique.[18,20–22] It is based on the sensitivity of the metal interband absorption on the energy distribution of the conduction electrons. In noble metals, absorption in the optical spectral range can be clearly separated into contributions due to intraconduction band transitions (quasifree electron absorption) and interband ones. The latter are dominated by transitions from the weakly dispersed full d bands to conduction band states and only take place above a certain threshold Ω_{ib}, with $\hbar\Omega_{ib} \approx 4$ eV in silver and 2.3 eV in gold [Fig. 1(a)]. In the equilibrium situation, it is roughly determined by the energy difference between the top of the d bands and the lowest-energy empty states in the conduction band, i.e., lying in the $k_B T_e^0$ energy range around the Fermi energy E_F, T_e^0 being the electron temperature. Heating up the conduction electrons or, more generally modifying their distribution reflects in changes of the electron occupation number f around E_F and thus of the interband absorption spectrum.

A transient perturbation can be created by intraband (free electrons) absorption of a femtosecond pulse of frequency ω_{pp} smaller than Ω_{ib}. If the pulse duration is smaller than the characteristic electron energy redistribution time, an athermal nonequilibrium electron distribution is selectively created [Fig. 1(b)].[20,23] Electron-electron scattering subsequently redistributes the energy in the electron gas leading to a hot Fermi distribution at $T_e > T_e^0$, corresponding to a large
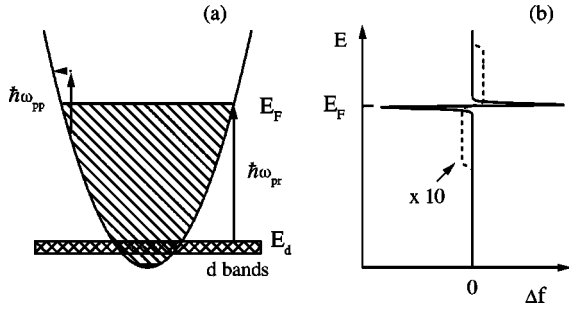
FIG. 1. (a) Schematic band structure of noble metals with a parabolic conduction band and flat d bands. The left arrow shows the intraband excitation process at $\hbar\omega_{pp}$ and the right one probing of the d band to conduction-band transitions at $\hbar\omega_{pr}$. The interband transition threshold is $\hbar\Omega_{ib} = E_F - E_d$, E_d being the energy of the top of the d bands. (b) Change of the electron state occupation number $\Delta f = f - f_0$ for a steplike initial distribution created by intraband electron absorption of a very short pulse (dashed line) and a thermalized one (full line) for the same electron gas energy increase (see Fig. 2).

occupation number change localized around E_F [Fig. 1(b)]. This evolution can be followed in the time domain, by a second time-delayed femtosecond pulse monitoring the buildup of the material optical response change around Ω_{ib}. The kinetics of the establishment of an electron temperature has thus been studied in gold and silver films.[20,22]

A similar approach can be used in noble-metal nanoparticles provided that they retain the main band-structure features of the bulk material [i.e., for sizes typically larger than 2–3 nm (Ref. 24)] and taking into account modification of the material optical properties by the dielectric confinement. The creation and kinetics of a nonequilibrium electron distribution and the induced optical property changes in a composite material formed by noble-metal nanoparticles dispersed in a matrix will be discussed in the following section on the basis of a bulklike model. In Sec. IV the theoretical results will be compared to the experimental ones obtained in silver and gold nanospheres with sizes ranging from 2 to 26 nm, embedded in different matrices. The size dependence of the observed internal thermalization times will be discussed in Sec. V, in terms of a simple model introducing surface effects on the electron-electron Coulomb interaction.

II. NONEQUILIBRIUM ELECTRON KINETICS

In femtosecond experiments, the metal electrons are first driven out of equilibrium by a pump pulse. In our measurements this is done by intraband absorption of a femtosecond pulse of frequency ω_{pp} well below the interband transition threshold, $\omega_{pp} < \Omega_{ib}$ [Fig. 1(a)]. Energy is selectively injected in the conduction electrons without modification of their density. During excitation, a coherent superposition of the electronic polarization and electromagnetic field of the pump pulse is initially created. Light absorption takes place with damping of this mixed material-field excitation by electron scattering leading to single electron excitation [Landau damping (Ref. 25)]. This process takes place on a sub 10 fs time scale as shown in second and third harmonic generation

experiments[26–28] and hole burning measurements.[29] On the time scale of our experiments performed with pulses in the 25–55 fs range (see Sec. III), coherent effects can thus be neglected and only energy redistribution processes have to be considered. Electron excitation can thus be globally described using the single-particle excitation model of free-electron absorption: one photon is absorbed by one electron with assistance of a third particle to conserve energy and momentum [Fig. 1(a)]. The concomitant instantaneous reduction of the occupation of electron states well below the Fermi energy, i.e., for $E_F - E \gg k_B T_e$, has been experimentally observed with 20 fs pulses, confirming the above picture.[23]

This excitation mechanism leads to a strongly athermal electron distribution with increase of the occupation of the electron states above E_F and decrease below it.[20–22] These distribution changes extend over a broad energy range of $2\hbar\omega_{pp} \gg 2k_B T_e$, where T_e is the electron temperature after internal thermalization [Fig. 1(b)]. Describing the conduction electrons by a one-particle distribution function f and assuming an isotropic parabolic conduction band,[30] the induced change at time t is given by

$$\frac{df^{exc}}{dt}(E,t) = BI_p(t)\{\sqrt{E - \hbar\omega_{pp}}\, f(E - \hbar\omega_{pp}, t)[1 - f(E,t)]$$

$$- \sqrt{E + \hbar\omega_{pp}}\, f(E,t)[1 - f(E + \hbar\omega_{pp}, t)]\}, \quad (1)$$

where E is the electron energy, I_p the pump pulse intensity and B a parameter describing the electron-photon coupling efficiency. If one could neglect electron energy relaxation during excitation, the nonequilibrium electron distribution would exhibit a steplike shape [Figs. 1(b) and 2(b), and 2(e)].

In a more realistic description one has to take into account the evolution of the electron distribution due to electron-electron (e-e) and electron-phonon (e-ph) scattering during the pulse duration. In bulk metals, the kinetics of the excitation and energy redistribution processes have been shown to be well described by the electron Boltzmann equation:[20,22]

$$\frac{df(E,t)}{dt} = \frac{df(E,t)}{dt}\bigg|_{e\text{-}e} + \frac{df(E,t)}{dt}\bigg|_{e\text{-}ph} + \frac{df^{exc}}{dt}(E,t). \quad (2)$$

The first and second terms on the right-hand side are the e-e and e-ph scattering rates, respectively.[22]

The time-dependent electron distribution functions computed in bulk silver using Eqs. (1) and (2) are shown in Figs. 2(g), 2(h), and 2(i) for a 25 fs pump pulse with $\hbar\omega_{pp} = 1.5$ eV. The build up of the induced distribution change amplitude $\Delta f(E,t) = f(E,t) - f_0(E)$ around E_F during the pump pulse duration is a consequence of the fast e-e scattering for electron states away from E_F (f_0 is the equilibrium electron distribution function at the initial temperature T_e^0).[22,31] This fast energy redistribution leads to a $\Delta f(E)$ shape distortion as compared to instantaneous excitation [Figs. 2(h) and 2(e)]. However, e-e scattering being strongly reduced close to E_F, the electron distribution stays athermal for few hundred femtoseconds.

Experimentally, it has been shown that establishment of a hot Fermi-Dirac distribution takes place with characteristic
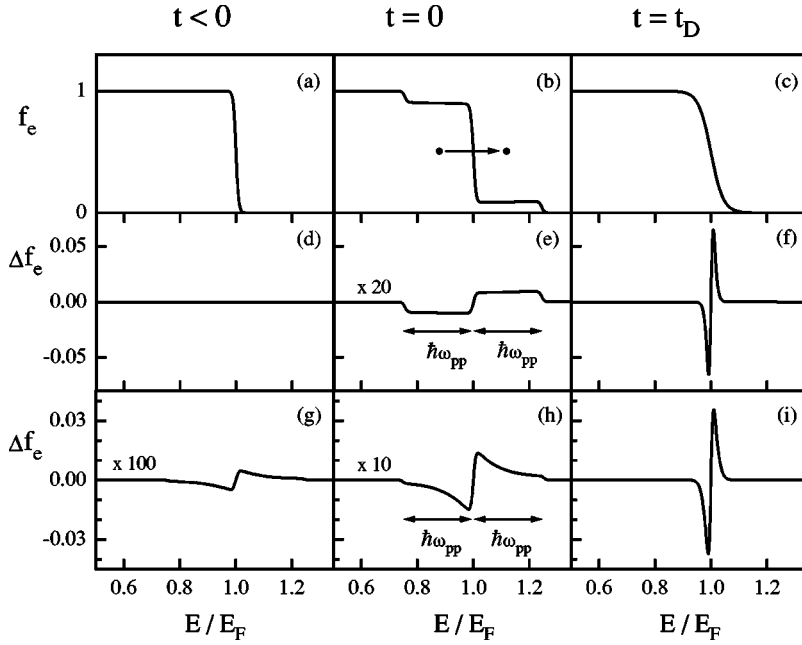
FIG. 2. (a) Energy dependent electron occupation number before excitation, $t < 0$ (equilibrium f_0), (b) during excitation (at $t = 0$ assuming instantaneous intraband excitation by a pump pulse of frequency ω_{pp}, with $\hbar\omega_{pp} = 0.24 E_F$), and (c) after establishment of an electron temperature after a delay $t = t_D > 0$. (d), (e), and (f) are the corresponding distribution changes $\Delta f = f - f_0$ for $\Delta T_e^{me} = 100$ K (the same total electron gas energy is assumed for (e) and (f)]. (g), (h), and (i) are the distribution changes computed at time $t = -30, 0$, and 400 fs for intraband electron excitation with a 25 fs pulse using the electron Boltzmann equation (2) taking into account e-e and e-ph scattering ($t = 0$ is the maximum of the pulse).

times $\tau_{th} \approx 350$ fs and ≈ 500 fs in bulk silver and gold, respectively.[20,22] These results have been quantitatively reproduced using the above electron kinetics model, introducing a phenomenologically reduced static screening of the e-e Coulomb potential. It accounts for screening overestimation using the static Thomas-Fermi model and has been done using an effective screening wave vector q_S instead of the Thomas-Fermi one q_{TF}:[22]

$$q_S = \beta q_{TF} = \beta \left(\frac{e^2 m^{3/2}}{\sqrt{2}\pi^2 \hbar^3 \varepsilon_0 \varepsilon_d} \int_0^\infty \frac{f(E)dE}{\sqrt{E}} \right)^{1/2}$$

$$\approx \frac{\beta e \sqrt{m}}{\pi\hbar\sqrt{\varepsilon_0\varepsilon_d}} (3\pi^2 n_e)^{1/6} \qquad (3)$$

with $\beta = 0.73$. n_e is the conduction electron density and ϵ_d the contribution of the d electrons to the static metal dielectric function. It accounts for their contribution to the screening of the conduction electron interactions, with $\epsilon_d = 6.7$ and 3.7 in gold and silver, respectively. These values have been extracted from the experimental complex dielectric function of the bulk materials[32–34] by a Kramers-Kronig analysis after subtracting the conduction-electron contribution fitted by a Drude-Sommerfeld expression.[22,35,36] The slower thermalization in gold than in silver is a consequence of the larger contribution of the d-band electrons to screening in gold (with $\tau_{th}^{Au}/\tau_{th}^{Ag} \approx \sqrt{\epsilon_d^{Au}/\epsilon_d^{Ag}}$ since $n_e^{Au} \approx n_e^{Ag}$, see Sec. V).[22]

The above electron kinetics modeling has been developed for bulk metals. As a first approximation, it can be used for interpreting the ultrafast response of not too small particles (at least for $D \gtrsim 2$–3 nm), taking into account enhancement of the e-e and e-ph scattering efficiencies.[12,18] As a rough approximation, this can be done by phenomenologically increasing the amplitude of the corresponding scattering rate in Eq. (2).

The large buildup of Δf around the Fermi energy concomitant with the establishment of the electron temperature can be followed in the time domain by a time-delayed probe pulse monitoring the sample optical transmission change $\Delta T(t_D)$, at the frequency ω_{pr} close to Ω_{ib} [$\Delta T(t_D)$ is the difference between the sample transmission at time t_D after the maximum of the pump pulse minus the one before perturbation]. To model the measured optical response one has first to connect the sample transmission to its dielectric constant and then the latter to the electron distribution function f.

In this work, we studied samples made of a large ensemble of nanoparticles dispersed in a liquid or solid matrix. For a low volume fraction $p \ll 1$ of small spheres ($D \ll \lambda$, where λ is the optical wavelength), the composite material optical properties can be described by an effective dielectric constant[15,25,37–41]

$$\tilde{\epsilon}(\omega) = \epsilon_m + 3p\,\epsilon_m \frac{\epsilon(\omega) - \epsilon_m}{\epsilon(\omega) + 2\epsilon_m}, \qquad (4)$$

where ϵ_m is the matrix dielectric constant, assumed frequency independent and real. The absorption coefficient can then be written:[39,40,42]

$$\tilde{\alpha}(\omega) = \frac{9\,p\,\epsilon_m^{3/2}}{c} \frac{\omega\,\epsilon_2(\omega)}{[\epsilon_1(\omega) + 2\epsilon_m]^2 + \epsilon_2^2(\omega)}, \qquad (5)$$

where $\epsilon(\omega) = \epsilon_1(\omega) + i\epsilon_2(\omega)$ is the dielectric function of the metal nanoparticles. As compared to the bulk metal, the absorption is resonantly enhanced close to the frequency Ω_R minimizing the denominator which is the condition for the surface-plasmon resonance (SPR) or Mie's resonance.[43] The absorption spectrum of noble-metal nanoparticles is well reproduced using Eq. (5) with the measured bulk dielectric constant[32,33] modified by a surface correction.[4] The resonance is taking place around $\hbar\Omega_R = 3$ eV, well below $\hbar\Omega_{ib}$,
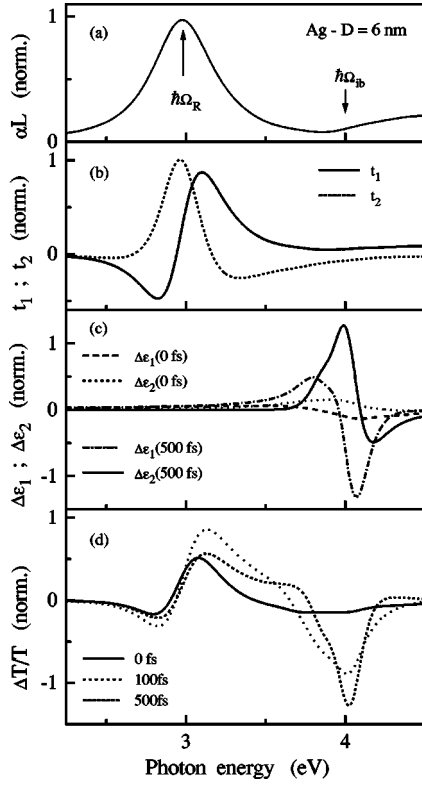
FIG. 3. (a) Fit to the measured absorption spectra of $D=6$ nm silver nanoparticles in BaO-P$_2$O$_5$. The SPR frequency ($\hbar\Omega_R = 2.98$ eV) and interband transition threshold ($\hbar\Omega_{ib} \approx 4$ eV) are indicated. (b) Dispersion of the coefficients t_1 and t_2 linking $\Delta T/T$ to $\Delta\epsilon_1$ and $\Delta\epsilon_2$ [Eq. (7)] for the same sample. (c) Interband contribution to $\Delta\epsilon_1$ and $\Delta\epsilon_2$ calculated for $t_D=0$ fs and $t_D=500$ fs for excitation with a 25 fs near infrared pulse and $\Delta T_e^{me}=100$ K. (d) Corresponding induced transmission change due to the interband contribution for $t_D=0$, 100, and 500 fs.

and around 2.4 eV, close to $\hbar\Omega_{ib}$, in the investigated silver and gold nanoparticle samples, respectively [Figs. 3(a) and 4(a)].

Using a perturbational approach, the sample transmission change $\Delta T/T$ is connected to $\tilde{\epsilon}$ by

$$\frac{\Delta T(t_D)}{T} = \frac{\partial \ln T}{\partial \tilde{\epsilon}_1} \Delta\tilde{\epsilon}_1(t_D) + \frac{\partial \ln T}{\partial \tilde{\epsilon}_2} \Delta\tilde{\epsilon}_2(t_D). \qquad (6)$$

In the dilute composite materials investigated here, $\Delta T/T$ is only determined by $\Delta\tilde{\epsilon}_2$, or, equivalently, by the sample absorption change:

$$\begin{aligned}
\Delta T/T(\omega_{pr}, t_D) &= -\Delta\tilde{\alpha}(\omega_{pr}, t_D) L \\
&= t_1(\omega_{pr}) \Delta\epsilon_1(\omega_{pr}, t_D) \\
&\quad + t_2(\omega_{pr}) \Delta\epsilon_2(\omega_{pr}, t_D), \qquad (7)
\end{aligned}$$

where L is the sample thickness. The coefficients $t_1 = -(\partial\tilde{\alpha}/\partial\epsilon_1)L$ and $t_2 = -(\partial\tilde{\alpha}/\partial\epsilon_2)L$ [Figs. 3(b) and 4(b)], are entirely determined by Eq. (5) and the ϵ values used for reproducing the linear absorption spectrum.
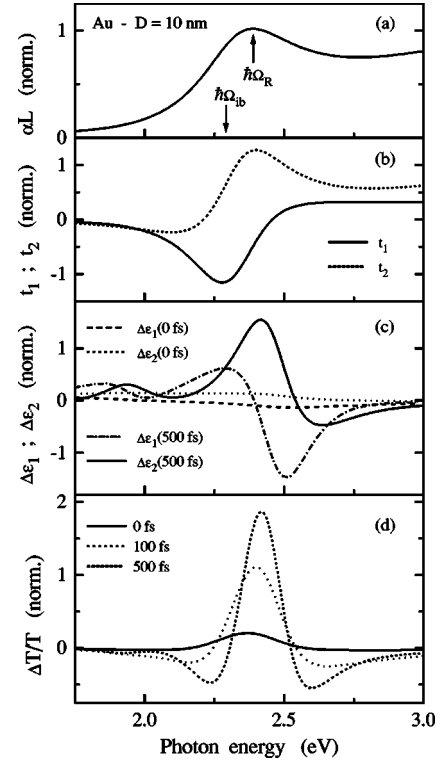
FIG. 4. Same as Fig. 3 for a $D=10$ nm gold colloidal solution. The SPR frequency is $\hbar\Omega_R=2.38$ eV and the interband transition threshold $\hbar\Omega_{ib} \approx 2.3$ eV.

Around the interband transition threshold Ω_{ib}, the change of the quasifree electron contribution to ϵ is small as compared to that of the interband one which dominates the response: $\Delta\epsilon \approx \Delta\epsilon^b$. To compute the optical response, one has thus to connect $\Delta\epsilon^b$ to Δf. This has been done in bulk silver and gold for interpreting continuous wave (CW) thermomodulation measurements, introducing model band structures around the Brillouin zone points yielding the larger contribution to the interband absorption.[44,45] In Ag, this takes place around the L point of the Brillouin zone, with a main contribution due to transitions from the d bands to the conduction band, and a weaker one, due to transition from the conduction-band to a higher energy empty s band.[44] In Au, only d band to conduction-band transitions are taking place, with a dominant contribution at the L point and a weaker one at lower energy around the X point.[45] The $\Delta\epsilon_1^b$ and $\Delta\epsilon_2^b$ spectra computed with these models for $t_D=0$ and 500 fs are shown in Figs. 3(c) and 4(c) for bulk silver and gold.

Band-structure changes being weak for the investigated nanoparticle sizes,[39] the induced $\Delta T/T$ in a nanoparticle sample can be calculated from the bulk metal $\Delta\epsilon = \Delta\epsilon^b$ using Eq. (7). In silver, $\Delta T/T$ exhibits two distinct spectral features around Ω_{ib} and Ω_R with different time behaviors [Fig. 3(d)]. The former is similar to the one in the bulk material. It corresponds to resonant probing of the interband transitions, the $\Delta T/T$ dispersion reflecting that of $\Delta\epsilon^b$. In contrast, the structure around Ω_R is specific to confined systems and is a consequence of the enhancement of the nonlinear optical response by the dielectric confinement around the SPR.[15] This reflects in the large amplitudes of t_1 and t_2

around Ω_R, amplifying the weak structureless $\Delta\epsilon^b$ response in this spectral range. In the case of gold, the SPR is close to Ω_{ib} and these two features overlap [Fig. 4(d)].

As expected, the computed $\Delta T/T$ around the interband transition threshold exhibits a strongly time-dependent shape in both silver and gold nanoparticles. For the athermal case ($t_D=0$ fs) a small $\Delta T/T$ amplitude with a broad structureless spectrum is obtained. It is in contrast with the quasithermal situation ($t_D=500$ fs) for which a strong peak is observed around $\hbar\Omega_{ib}$. Note that in gold nanoparticles, the maximum amplitude is blue shifted as compared to $\hbar\Omega_{ib}$ due to enhancement of the signal by the dielectric confinement effect. In both systems, the rise of the $\Delta T/T$ amplitude around $\hbar\Omega_{ib}$ is delayed and does not follow energy injection by the pump pulse. It is particularly clear in the case of silver where, in contrast, the structure around the surface-plasmon resonance frequency exhibits an almost instantaneous rise, as it is almost proportional to the electron gas excess energy.[21,46] This delayed rise reflects the buildup of Δf close to E_F, i.e., the internal electron thermalization dynamics, permitting to follow the electron thermalization in the time domain.

III. EXPERIMENTAL SETUP

The time-resolved transmission change experiments were performed using a high sensitivity femtosecond pump-probe setup. It is based on a home made Ti:sapphire oscillator tunable in the 1.07–0.82 μm range. The pulse duration is typically in the 25 fs range except for the longer wavelengths above 1 μm for which it increases up to a maximum of about 40 fs. Part of the output of the laser was used as the near-infrared pump (some measurements in Ag have also been performed by frequency doubling it). The second part was used to create the probe pulses either in the UV or green spectral range, in the vicinity of the silver and gold interband transition thresholds, about 310 and 530 nm, respectively. The green pulses were created by frequency doubling the fundamental pulses in a 100 μm thick BBO crystal. The UV pulses were generated by frequency doubling followed by sum frequency generation in BBO crystals.[22] After recompression in fused silica prism pairs, the pulse durations were about 40 and 55 fs in the green and UV ranges, respectively. The excitation process being nonresonant, it is weakly sensitive to the pump wavelength. Probe photon energy dependent measurements were thus performed by changing the operating wavelength of the oscillator.

The two beams were sent into a standard pump-probe setup, with mechanical chopping of the pump beam at 1.5 kHz and differential and lockin detection of ΔT. Taking advantage of the high stability and high repetition rate (76 MHz) of the oscillator, very high sensitivity measurements were performed with a noise level for $\Delta T/T$ in the 10^{-6} range. This sensitivity is important to study metallic systems in the weak perturbation regime (near-infrared pump fluences in the 5–200 μJ/cm^{-2} range). As usually done, the energy injected by the pump pulse is characterized by a maximum equivalent electron temperature rise ΔT_e^{me} defined as the temperature increase of a thermalized electron gas for the same injected energy. In the experiments described here ΔT_e^{me} is of the order of 50–400 K. The electron heat capacity being much smaller than the lattice one, the final temperature rise of the fully thermalized electron-lattice system is typically 1 K.

Experiments were performed in different samples made of silver or gold spherical nanocrystals dispersed in different matrices or deposited on a substrate. The first set of samples consists of silver nanoparticles embedded in a 50BaO-50P$_2$O$_5$ glass. They were prepared by a fusion and heat treatment technique.[47] The mean particle diameter D ranged from 4 to 30 nm. The metal volume fraction p was between 1×10^{-4}–5×10^{-4} with a sample thickness $L \approx 15$ μm. A second set of samples, formed by silver or gold clusters in Al$_2$O$_3$, was grown by low-energy cluster beam deposition with co-deposition of alumina on a silica substrate.[48] The mean size was in the 3–4 nm range and p typically a few percents. The thickness L of the cluster doped layer was about 0.2 μm. The third set of samples were silver or gold colloidal solutions in a 1 mm thick cell. They were prepared by chemical synthesis using a reverse micelle technique (Ag, with $D=5.8$ nm)[49] or a modified tannic acid/citrate method (Au, with $D=5,10$ or 20 nm).[50] The thiol stabilized particles were either left in solution (Au case) or deposited on a glass substrate (Ag case). All samples were characterized by transmission electron microscopy. They have narrow size dispersion with standard size deviations ranging from 4 to 10% of D but for the Al$_2$O$_3$ matrix samples (about 30%).

IV. ELECTRON ENERGY EXCHANGES: SIZE EFFECT

The probe wavelength dependence of $\Delta T/T$ measured around $\hbar\Omega_{ib}$ in the $D=6$ nm silver sample is shown in Fig. 5(a) for two pump-probe time delays: $t_D=0$ and 400 fs. The measured spectral shapes are in good agreement with the computed ones. In particular, they exhibit the same narrowing with time and concomitant large increase of the $\Delta T/T$ amplitude around $\hbar\omega_{pr}\approx 4$ eV. This confirms that the measured signal can be entirely ascribed to modification of the interband transition spectrum. As in films for CW and transient measurements,[20,22,45,51] a slightly broader experimental than calculated shape is observed. This deviation can be ascribed to the approximations made in the band-structure modeling and/or neglect of the width of the electronic states.

The spectral shape narrowing of $\Delta T/T$ is accompanied by sign changes with time on its blue and red wings [Fig. 5(a)]. They are better seen by plotting the measured time dependence of $\Delta T/T$ for a fixed probe wavelength [Fig. 6(a)]. The observed complex temporal and spectral behaviors are in good agreement with the computed ones [Fig. 6(b)] and similar to those previously reported in silver films.[22] They are signatures of the existence of a non-Fermi electron distribution in metal nanoparticles on a few hundred femtosecond time scale, i.e., a delayed electron gas internal thermalization.

Similar shapes were observed for all the investigated Ag samples [Fig. 5(b)] with a narrowing of the red wing with size reduction. It is a consequence of the size dependence of
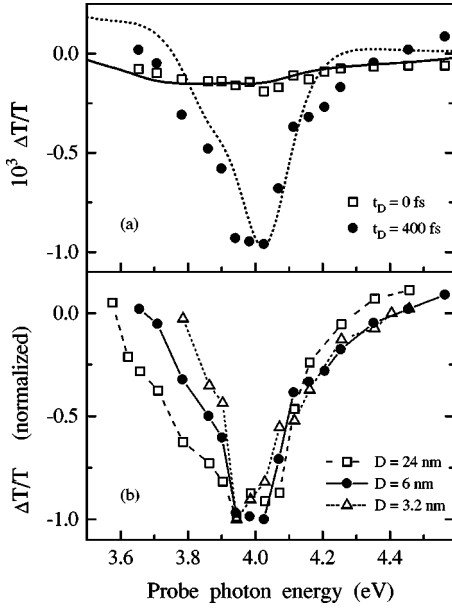
FIG. 5. (a) Probe photon energy dependence of the transmission change $\Delta T/T$ measured around the interband transition threshold $\hbar\Omega_{ib}$ for pump-probe delays of 0 fs and 400 fs in $D=6$ nm Ag nanoparticles in BaO-P$_2$O$_5$. The pump fluence is 180 μJ/cm^2. The full and dashed lines are calculated from the transient electron distribution (see Sec. II). (b) same as (a) for a pump-probe delay of 400 fs and $D=24$ and 6 nm Ag nanoparticles in BaO-P$_2$O$_5$ and $D=3.2$ nm Ag clusters in Al$_2$O$_3$. The lines are only connecting the experimental points.

the optical response of the material, i.e., of the t_1 and t_2 coefficient in Eq. (7). Physically, it is due to the influence of the SPR on the nonlinear optical response, the positive SPR induced $\Delta T/T$ contribution partly balancing the negative one associated with the interband transition in this spectral range [Fig. 3(d)]. As the SPR width increases for small nanoparticles, its contribution on its blue wing increase, blue shifting
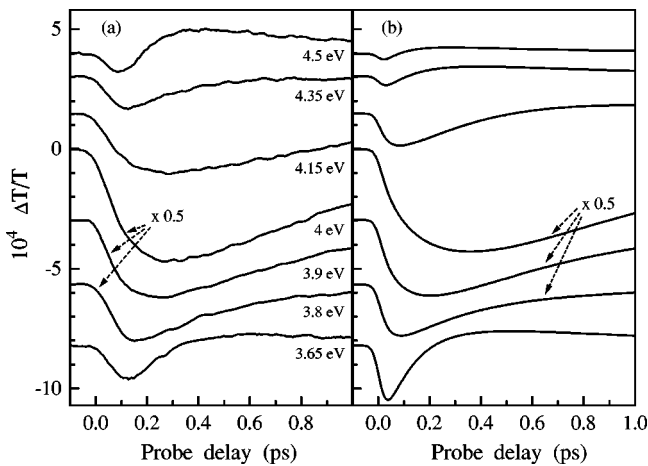
FIG. 6. (a) Time-dependent transmission change $\Delta T/T$ measured in $D=6$ nm Ag nanoparticles in BaO-P$_2$O$_5$ for different probe photon energies as indicated in the figure. (b) Corresponding $\Delta T/T$ computed using the calculated electron distribution function and the bulk silver band-structure model (see text).
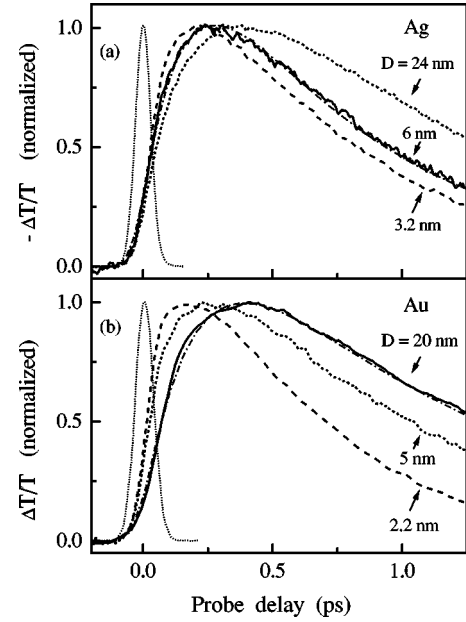
FIG. 7. (a) Time behavior of the transmission change $-\Delta T/T$ measured for $\hbar\omega_{pr}\approx3.95$ eV and $\hbar\omega_{pp}\approx1.32$ eV in spherical Ag nanoparticles of diameter $D=24$ nm and 6 nm in BaO-P$_2$O$_5$ and $D=3.2$ nm in Al$_2$O$_3$. (b) Time dependent $\Delta T/T$ measured in $D=20$ and 5 nm gold colloidal solutions and $D=2.2$ nm clusters in a Al$_2$O$_3$ matrix. The dash dotted lines in (a) and (b) are fits to the Ag-$D=6$ nm and Au-$D=20$ nm cases using Eq. (8). The dotted lines are the pump-probe cross correlations.

the spectral position of the $\Delta T/T$ sign change. The similar $\Delta T/T$ spectral shapes measured in the different samples confirm that band-structure modifications are negligible for the investigated particle sizes and that they are probed in similar conditions. This is making possible a direct comparison of the measured $\Delta T/T$ temporal behavior in the different composite materials.

This can be done by monitoring the spectral shape narrowing of $\Delta T/T$ around $\hbar\Omega_{ib}$ or, equivalently, the rise of the $\Delta T/T$ maximum amplitude around 4 eV. The results obtained for $\hbar\omega_{pr}\approx3.95$ eV and $\hbar\omega_{pp}\approx1.32$ eV are plotted in Fig. 7 for $D=3.2$, 6, and 24 nm, together with the pump-probe cross correlation. In all samples, $\Delta T/T$ exhibits a clearly resolved rise time that decreases with the nanoparticle size.

The probe photon energy dependence of $\Delta T/T$ measured in $D=20$ nm gold colloidal solution is shown in Fig. 8(b) for two time delays. The observed shape is similar to that previously reported in the strong excitation regime.[7,10,11,52,53] It is in very good quantitative agreement with the computed response based on the bulk gold band-structure model of Rosei [Fig. 8(b)]. As in silver, the response can thus be entirely ascribed to modification of the interband transition spectrum with minor contribution from other effects.[54,55] A delayed rise of the $\Delta T/T$ signal is also clearly observed demonstrating a slow electron thermalization kinetics.

However, in contrast to silver, the spectral shape in gold is determined not only by the dispersion of $\Delta\epsilon^b$ but also by that of the SPR enhancement effects [Fig. 4(d)]. In particular, the position of the maximum $\Delta T/T$ amplitude is here correlated
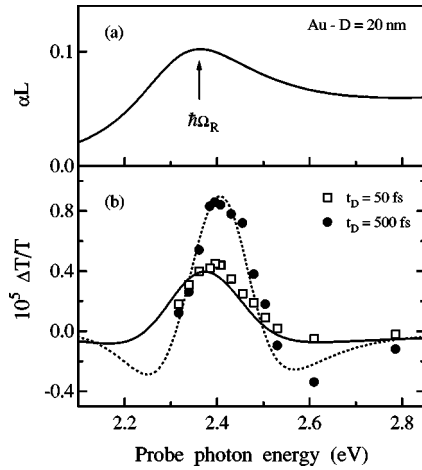
FIG. 8. (a) Fit to the measured absorption spectra of $D = 20$ nm gold colloid. The SPR frequency $\hbar\Omega_R$ is indicated. (b) Probe photon energy dependence of the transmission change $\Delta T/T$ measured for pump-probe delays of 50 fs and 500 fs. The full and dashed lines are calculated from the transient electron distribution (see Sec. II).

to the SPR frequency rather than to $\hbar\Omega_{ib}$, and slightly blue shifts during internal electron gas thermalization [Fig. 8(b)]. As in copper,[6] it makes the $\Delta T/T$ temporal behavior sensitive to the probe wavelength around the SPR frequency in good qualitative agreement with our modeling, as illustrated in Fig. 9. In order to compare the $\Delta T/T$ kinetics in different samples and in films the measured shapes have thus been compared for a fixed probe photon energy $\hbar\omega_{pr} = 2.4$ eV. The results are shown in Fig. 7(b) for $D = 20$ and 5 nm gold nanoparticles in solution and for $D = 2.2$ nm gold cluster in an alumina matrix.
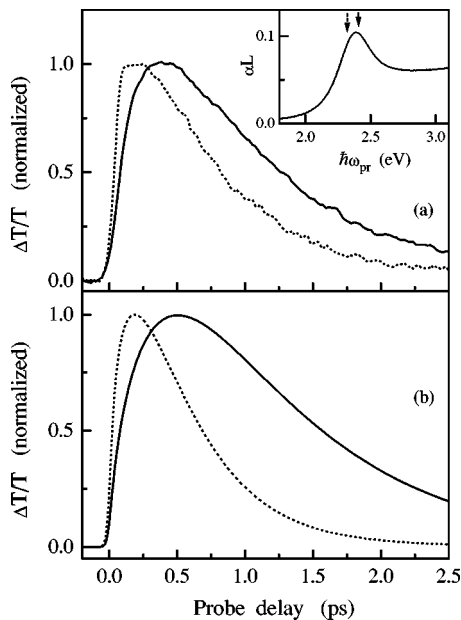
FIG. 9. Measured (a) and calculated (b) normalized transmission change $\Delta T/T$ in $D = 20$ nm gold colloid for $\hbar\omega_{pr} = 2.33$ eV and 2.41 eV (dashed and full line, respectively). The inset shows the colloid absorption spectrum and the probe photon energies (arrows).
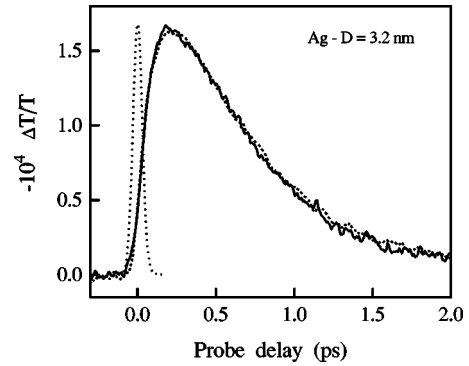
FIG. 10. Time behavior of the transmission change $-\Delta T/T$ measured in $D = 3.2$ nm Ag particles in Al_2O_3 with near infrared ($\hbar\omega_{pp} \approx 1.32$ eV, dashed line), or blue ($\hbar\omega_{pp} \approx 2.64$ eV, full line) pump pulses. The probe photon energy is $\hbar\omega_{pr} \approx 3.95$ eV. The dotted line is the pump-probe correlation function for the infrared pump—UV probe case.

Pauli exclusion is a key factor in the slow thermalization kinetics measured here. It leads to blocking of the final states for electron scattering, strongly decreasing the probability of the e-e collisions around the Fermi energy. It is directly related to the occupation of the electron states $f(E,t)$ and can be strongly modified by the pump pulse. It has been shown that the thermalization dynamics is independent of the injected energy in the weak perturbation regime, i.e., ΔT_e^{me} smaller than typically 300 K. Smearing of the electron distribution around E_F is then sufficiently small to neglect alteration of the e-e scattering rate. It is perturbation dependent for larger energy injection leading to a fastening of the signal rise.[22] The results obtained as a function of the nanoparticle size and environment can thus be compared only if the measurements are always performed in the weak excitation regime, i.e., if the observed kinetics is independent of the excitation amplitude.

As usually done, we have checked that our results are independent of the pump fluence. However, below a certain fluence level, less than one photon is on average absorbed per nanoparticle. In this regime, which is reached for the smallest particles we are investigating, further pump fluence reduction only reduces the number of excited particles, not their excitation amplitude. It is set by the minimum energy injected in a particle, i.e., one photon $\hbar\omega_{pp}$. This minimum excitation induces a large temperature rise in small particles, $\Delta T_e^{me} = 360$ K and 610 K for $\hbar\omega_{pp} = 1.3$ eV and 2.6 eV, respectively, in a $D = 3.2$ nm Ag particle. To check that the time response is independent of the excitation amplitude, we have performed additional measurements as a function of the pump photon energy. Identical results were obtained in the $D = 3.2$ nm Ag particle sample using pump pulses either at the fundamental, $\hbar\omega_{pp} \approx 1.32$ eV, or second harmonic, $\hbar\omega_{pp} \approx 2.64$ eV, of the femtosecond oscillator for the same probe photon energy $\hbar\omega_{pr} \approx 3.95$ eV (Fig. 10). Note that though the nonequilibrium distributions are initially different, for the two excitation conditions, the high-energy electron states relax in few femtoseconds. They very weakly influence the observed kinetics on the considered time scale that is thus identical for the two excitation conditions. This is

in agreement with our simulations and with the fact that the observed behavior is essentially governed by electron scattering close to the Fermi energy.

As previously done in metal films,[20,22] a more quantitative comparison of the measured $\Delta T/T$ responses at the characteristic frequency $\hbar\omega_{pr}=4$ eV in Ag and 2.4 eV in Au, can be performed by defining an internal thermalization time τ_{th}. It is determined by fitting the experimental results by a response function u with the form

$$
\begin{aligned}
u(t) = H(t)\{ &A[1-\exp(-t/\tau_{th})]\exp(-t/\tau_{e-ph})\\
&+B[1-\exp(-t/\tau_{e-ph})]\},
\end{aligned} \tag{8}
$$

where $H(t)$ is the Heaviside function. The first term describes the purely electronic response which rises with the time constant τ_{th} and decays by electron energy transfer to the lattice with the effective electron-phonon coupling time τ_{e-ph}. The second term account for the small residual signal ($B<A/10$) due to heating of the lattice and rising with the time constant τ_{e-ph}. B is determined by the long time delay (few picoseconds) measurements. τ_{e-ph} has been shown to decrease with size in Ag and Au nanoparticles.[12] This effect is fully accounted for here by using τ_{e-ph} as a fitting parameter that is determined by the long delay $\Delta T/T$ behavior, not influenced by τ_{th}. The obtained τ_{e-ph} values are in good agreement with the previously reported ones.[12] A good reproduction of the $\Delta T/T$ time behavior is obtained by convolving the measured pump-probe cross correlation with u as shown in Fig. 7(a) for the $D=6$ nm silver sample using $\tau_{th}\approx250$ fs and in Fig. 7(b) for the $D=20$ nm Au sample using $\tau_{th}\approx450$ fs. This is significantly smaller than the bulk value measured in optically thin silver films, $\tau_{th}\approx350$ fs and comparable in the gold case, $\tau_{th}\approx500$ fs. The rise time is found to be slower in gold than in silver, in agreement with the bulk metal results.[20,22]

The size dependence of the measured τ_{th} is very similar in silver and gold nanoparticles as shown in Fig. 11. For sizes larger than 10 nm, τ_{th} is comparable to the one determined in metal films, indicating a weak confinement effect for these sizes. This is consistent with the results of previous measurements in $D=9$ and 48 nm gold colloids, that yield τ_{th} values almost identical to the bulk gold one.[56] For smaller sizes, τ_{th} strongly decreases eventually reaching a value three to two times smaller than the bulk metal one for 2–3 nm clusters, i.e., 250–820 atoms (Fig. 11).

The results obtained for nanoparticles prepared by different techniques and embedded in different solid matrices, or in solution with surface bound thiols, or deposited on a substrate are very similar. This clearly demonstrates that the observed τ_{th} variation is independent of the environment and sample preparation method. The observed fastening of the electron thermalization with size reduction can thus be ascribed to an intrinsic effect, i.e., confinement induced increase of the electron energy exchanges in small metal nanoparticles.
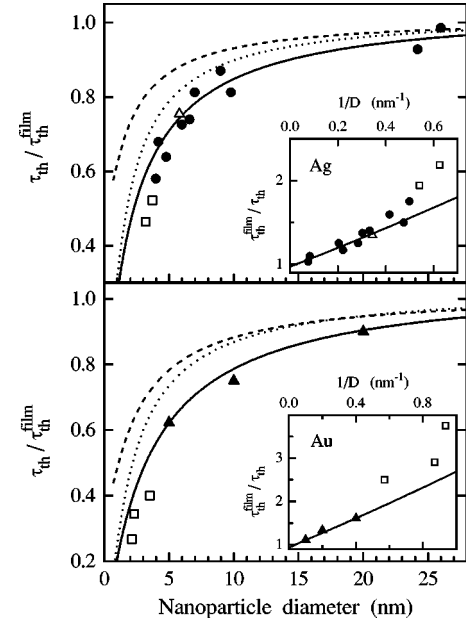
FIG. 11. Size dependence of the electron thermalization time τ_{th} for Ag (a) and Au (b) nanoparticles embedded in a BaO-P_2O_5 (full dots) or Al_2O_3 (open squares) matrix, deposited on a substrate (open triangle) or in colloidal solution (full triangles). All the data are normalized to the measured metal film values τ_{th}^{film}. The full lines are the computed τ_{th} taking into account both the spillout and d-electron localization effects. The dashed and dotted lines are calculated suppressing the spillout or d-electron surface effect, respectively. The insets show the same data for the normalized thermalization rate $\tau_{th}^{film}/\tau_{th}$ as a function of the inverse diameter D^{-1}.

V. ELECTRON ENERGY EXCHANGES: MODELING

Within the Fermi liquid theory,[57] the two-body electron-electron (e-e) interaction is expressed by a Coulomb potential screened by both the conduction and bound electrons (d electrons in noble metals). This permits a good reproduction of the transient dynamics of the one-electron distribution function f in bulk metals (Sec. II).[20,22] In this approach, the scattering rate $\gamma_{ee}(E)$ of an electron out of its E energy state due to e-e collision is given by[22,57–61]

$$
\begin{aligned}
\gamma_{ee}=\tau_{ee}^{-1}=&\frac{me^4}{64\pi^3\hbar^3\epsilon_0^2\epsilon_d^2 E_S^{3/2} E_F^{1/2}}\left[\frac{2\sqrt{E_F E_S}}{4E_F+E_S}+\arctan\sqrt{\frac{4E_F}{E_S}}\right]\\
&\times(E-E_F)^2,
\end{aligned} \tag{9}
$$

where $E_S=\hbar^2 q_S^2/2m$ and energy is measured from the bottom of the conduction band. The various quantities E_F, E_S, and q_S depend only on the effective electron mass m, the conduction electron density n_e, and the static background dielectric function, i.e., the interband term $\epsilon_d(\omega=0)$ in bulk metal. The scattering amplitude for a fixed electron energy is completely determined by these parameters. For a fixed mass, $m\approx m_0$, the free electron mass, in Ag and Au, the n_e and ϵ_d dependences of γ_{ee} are given by

$$\gamma_{ee} \propto n_e^{-5/6} \epsilon_d^{-1/2} \left[\frac{2\sqrt{E_F E_S}}{4E_F + E_S} + \arctan \sqrt{\frac{4E_F}{E_S}} \right] \propto n_e^{-5/6} \epsilon_d^{-1/2}. \tag{10}$$

The term in bracket being almost constant, the main dependences are included in the first two terms.[18]

As discussed in Sec. II, the experimental electron thermalization time τ_{th} reflects the energy redistribution inside the electron gas after absorption of a femtosecond pulse. It is determined by the e-e scattering events over a certain energy range, actually mostly in the vicinity of the Fermi surface where the slowest processes underlying the electron dynamics are taking place. The thermalization rate τ_{th}^{-1} is thus expected to be proportional to the e-e collision probability γ_{ee} and to exhibit the same n_e and ϵ_d dependences. This has been confirmed by numerical simulation of the electron thermalization kinetics in bulk metals using the model of Sec. II. Furthermore, the predicted variation with $\sqrt{\epsilon_d}$ is in very good agreement with the experimentally measured τ_{th} increase from silver to gold films ($\sqrt{\epsilon_d^{Au}/\epsilon_d^{Ag}} \approx 1.35$ and $\tau_{th}^{Au}/\tau_{th}^{Ag} \approx 1.4$).[22]

The spatial distributions of both the conduction and d band electrons are no more homogeneous in a cluster since they are modified close to the surfaces. The conduction electron wave functions extend beyond the classical particle size of radius $R_N = r_s N^{1/3}$ where N is the number of atoms in the cluster and r_s the Wigner-Seitz radius $r_s^3 = 3/(4\pi n_e)$. The density n_e thus decreases close to the inner surface of the cluster and presents a tail extending outside.[62–65] This electron spillout effect is responsible for the red shift of the surface-plasmon resonance frequency with size reduction observed in small alkalin clusters.[66] Conversely, the d electron wave functions are localized in the inner region of the particle leading to an incomplete embedding of the conduction electrons in the core electron background.[67–70] These two effects are responsible for the tiny surface-plasmon resonance blue shift observed in small noble-metal clusters (i.e., on the linear optical properties).[69,70] This is the net result of the competing red- and blue-shift trends resulting from the spillout effect and surface skin of ineffective d electron polarizability (with the possible additional influence of local background polarizability of the matrix out of the particle).[70] These effects modify two important parameters entering the bulk electron scattering rate: the electron density and d electron screening close to a surface[71,72] and are expected to be responsible for the observed increase of the effective e-e scattering rate in small nanoparticles.

Alteration of the electron distributions close to a surface has been modeled in the framework of a semiquantal multilayered model of jellium type (i.e., the discrete structure is disregarded). It yields a very good reproduction of the absorption spectra of various matrix-embedded noble-metal clusters.[70] The time-dependent local-density-approximation formalism was used for the linear optical properties and $n_e(r)$ obtained by solving the Kohn-Sham equations in the density-functional theory (DFT)(Fig. 12). In the inner region of the particle, $n_e(r)$ shows Friedel oscillations but stays very close to the bulk density, n_e^0. It exhibits a smooth de-
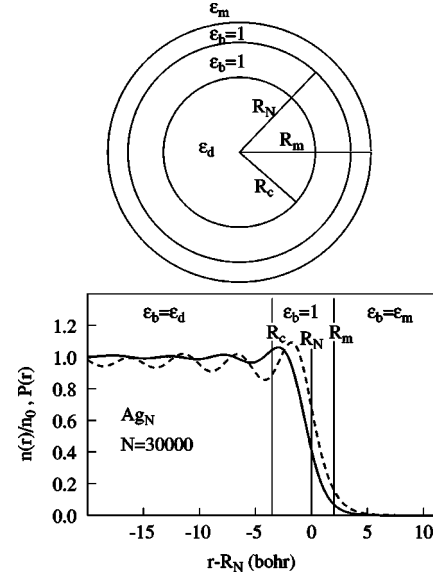
FIG. 12. Upper figure: Multilayered particle model used for estimating the τ_{th} size dependence. $R_N = r_s N^{1/3}$ is the particle radius (radius of the ionic background). $R_c = R_N - d$ is the radius of the medium with background dielectric function $\epsilon_b = \epsilon_d(\omega)$. $R_m = R_N + d_m$ is the radius beyond which the embedding matrix extends [$\epsilon_b = \epsilon_m(\omega)$]. In the intermediate zone [R_c, R_m] ϵ_b is equal to unity. In the standard calculations $d = 3.5$ a.u. and $d_m = 2$ a.u. are used.[70] Lower figure: the full line curve is the electronic density n_e normalized to the bulk metal one n_e^0 for the Ag$_N$ cluster with $N = 3 \times 10^4$ ($D \approx 10$ nm). The dashed line is the average electron density probability $P(r)$ corresponding to the single-electron states lying in the energy range [$E_F - 0.5$ eV, $E_F + 0.5$ eV].

crease in a region of a few a.u. around the surface. The density and its spatial profile in a cluster are almost identical for both Ag and Au whose conduction electron properties are very similar. Calculations performed for different sizes show that the surface profile of $n_e(r)$, including the outermost Friedel density oscillations, is to a large extent independent of the cluster size. This property holds true with respect to the effective potential well confining the conduction electrons. In the spillout region this feature stems from the fact that the surface profile is determined by the exponentially decreasing tails of the electronic wavefunctions [$n_e(r)$ is thus almost insensitive to the set of the occupied Kohn-Sham orbitals]. This feature permits to obtain by a simple radial scaling the electron density for each cluster size R_N from the self-consistent surface density profile calculated for a given large size.

The d-electron polarizability modification was described by a multilayered model, which involves three geometrical interfaces (Fig. 12). $R_c = R_N - d$ defines the radius of the inner bulklike metal region, characterized by the interband dielectric function: $\epsilon_b = \epsilon_d$ for $r < R_c$. $R_m = R_N + d_m$ is the radius beyond which the surrounding matrix extends. In this outer region, the background polarizability is determined by the matrix dielectric constant and ϵ_d has to be replaced by ϵ_m: $\epsilon_b = \epsilon_m$ for $r > R_m$. In the intermediate region $R_c < r < R_m$ no d electron or matrix contribution takes place: $\epsilon_b = 1$. In the inner region [$R_N - d, R_N$], it accounts for exclu-

sion of the d electrons from a surface layer of effective thickness d.[67-69] The vacuum shell of thickness d_m beyond R_N is introduced to mimic the spherically averaged local matrix porosity at the interface (surface roughness, contact defects, ...).[70] The values of the two effective parameters, $d = 3.5$ a.u. and $d_m = 2$ a.u. have been independently estimated in analyzing surface-plasmon resonance spectra in free Ag_N^+ clusters[69] and composite Ag_N:alumina samples.[70] Let us remark that identical d values are expected for Au and Ag particles since they have almost identical r_s values ($r_s \approx 3$ a.u.) and the long range part of the $4d$ and $5d$ wave functions are quite similar in Ag and Au atoms, respectively. In contrast, the d_m parameter is not an intrinsic one and *a priori* depends on the composite metal-matrix system and sample elaboration conditions.

To estimate the impact of the above effects on the electronic thermalization time in small metal particles and its correlation to the film one, we have used the bulk metal approach and phenomenologically introduced them as corrections.[18] This has been done by using a simple model consisting in spatially averaging the bulklike local scattering rate in the metal particle. In a spherical cluster the effective electronic thermalization time τ_{th} is thus estimated from

$$\tau_{th}^{-1} = \frac{\int_0^\infty 4\pi r^2 \{\tau_{th}^h(\epsilon_b(r), n_e(r))\}^{-1} g(r) dr}{\int_0^\infty 4\pi r^2 g(r) dr}, \quad (11)$$

where τ_{th}^h is the thermalization time for a homogeneous medium of electron density $n_e(r)$ and static background dielectric constant $\epsilon_b(r)$, with $\tau_{th}^h \propto \gamma_{ee}^{-1}$ Eq. (10). $g(r)$ is an appropriate weighting function, taken here equal to $n_e(r)$ as a first approximation.[18]

This local approach can be supported by a classical picture: the scattering rate at **r**, along the trajectory of the excited electrons, is assumed to be determined by $n_e(\mathbf{r})$ and $\epsilon(\mathbf{r})$ (i.e., the local electron gas density and background polarizability at **r**). This crude approximation can be justified to some extent by the short screening length of the Coulomb interaction (on the order of 2–3 a.u. in metals).

The size dependence of the thermalization times in silver and gold particles, calculated with the present model, are displayed in Fig. 11 (full lines). The full multilayered description has been used ($d = 3.5$ a.u. and $d_m = 2$ a.u.), with the static dielectric constant of bulk alumina [$\epsilon_m(0) = 9.5$] in the matrix region. The theoretical values have been normalized to the film one calculated using a similar model in a two-dimensional (2D) geometry. No fitting parameter has been introduced since all the constants were independently determined from previous spectral-domain measurements. In both metals the size-dependent experimental times are well reproduced by the theoretical predictions, over the entire size range with only a slight deviation for the smallest sizes. The good agreement between theory and experiment suggests that the observed enhancement of the e-e interactions in small particles can be ascribed to local reduction of the screening efficiency of the Coulomb potential close to the

surface. This surface induced enhancement of the e-e scattering is consistent with the larger surface than bulk electron state dephasing rate measured using a space-resolved technique.[22,73]

As every surface induced effects for not too small particles, its contribution varies as the ratio of the surface to bulk atom numbers, i.e., as $1/D$. This is rising from about 10% for $D = 10$ nm to about 50% for $D = 2$ nm. At least for the largest particles, for which the surface effects can be introduced as corrections, their efficiency is proportional to the surface to volume ratio, i.e., to the inverse diameter. This is illustrated in the insets of Fig. 11 showing the experimental and calculated thermalization rate τ_{th}^{-1} as a function of $1/D$. Note that the τ_{th} computed in the film with surface effects in 2D geometry is larger than the one in very large particle where no surface effect is taking place.

To yield some insights on the relative influence of the spillout and d-electron surface exclusion effects, we have computed the τ_{th} size dependence for only one or the other contribution, i.e., no surface layer, $d = 0$, or no spillout $n_e(r) = n_e^0$ for $r < R_N$ and $n_e(r) = 0$ for $r > R_N$, the other parameters being unchanged (Fig. 11). The results show that both ingredients are necessary to reproduce the measured dependence, the spillout effect giving the larger contribution for small sizes. The spillout contribution is about 60% (20%) larger than the surface layer related one for $D = 5$ nm Ag (Au) clusters. ϵ_d being larger in gold than in silver, the d electron related contribution is larger in the former, leading to an overall larger size dependence of τ_{th} (Fig. 11). Finally, let us remark that both effects lead to an increase of the electron-scattering rate whereas they yield opposite size trends with respect to the frequency shift of the surface-plasmon resonance.

The above "standard" parameters correspond to the case of the alumina embedded clusters. The experimental data involving particles embedded in different environments, we have studied the dependence of the estimated times on the environment parameters, i.e., $\epsilon_m(0)$ and d_m. For the two extreme cases of fully alumina-embedded clusters ($d_m = 0$) or clusters in vacuum ($\epsilon_m = 1$; or equivalently d_m very large), the thermalization times remain close to those calculated within the "standard" model (Fig. 13). This weak dependence is consistent with the experimental conclusion that the observed size dependence of the thermalization time is essentially ruled by intrinsic processes.

The computed relative variation of τ_{th} with $\epsilon_m(0)$ and d_m can be related to the background dielectric constant environment explored by the spillout electrons. It can be inferred in remarking that (i) the averaged value expressed by Eq. (11) is dominated by the zones where the local scattering rate is large (small ϵ_b value), and, (ii) the spillout effect, leading to a large increase of the scattering rate in the low electron density tail (reduction of n_e), can be noticeably counterbalanced in the matrix zone if it has a large ϵ_b. This partial quenching of the spillout induced increase of the scattering rate by the matrix-induced screening, is illustrated by the model results obtained for a very large matrix screening cor-
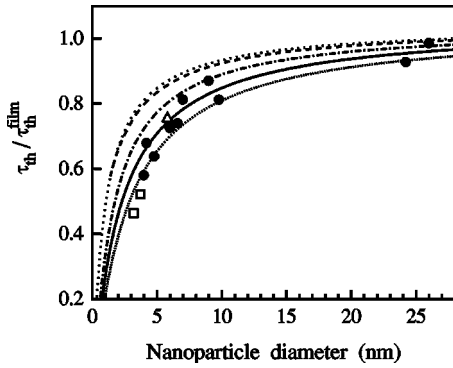
FIG. 13. Sensitivity of the computed τ_{th} to various parameters for silver nanoparticles. The full line shows the standard calculation results ($d=3.5$ a.u. and $d_m=2$ a.u.) for alumina-embedded clusters ($\epsilon_m=9.5$) with the weighting function $g(r)=n_e(r)$, Eq. (11). The other curves are computed in modifying one of the parameters or conditions: short-dot line (lower curve), $\epsilon_m=1$ (particles in vacuum); dashed-dotted line, $d_m=0$ (no local porosity), dotted line (upper curve), $d_m=0$ and $\epsilon_m=80$ (particles in water). The dashed line is computed using the weighting function $g(r)=P(r)$, and spatially averaging only E_S and ϵ_d.

responding to the case of metal nanoparticles fully embedded in water ($\epsilon_m=80$ and $d_m=0$, Fig. 13).

The weighting function g in Eq. (11) has been identified with the electron density n_e. This approach consist in modeling the spherical cluster as an ensemble of independent nested spherical metallic layers with specific electronic density $n_e(r)$ and background dielectric constant $\epsilon_b(r)$. However, owing to the Pauli's exclusion principle only nanoparticle electronic states with energy close to E_F are involved in the scattering processes. Another choice of the weighting function could thus be the density probability $P(r)$ $\propto|\psi(r)|^2$ of the electronic states in the vicinity of E_F. In this second averaging procedure the particle is considered as a whole: the excited electrons explore radial zones having a specific screening efficiency and only the quantities entering in the screening of the Coulomb interaction are averaged, i.e., ϵ_b and $E_S(n_e)$.

$P(r)$ has been determined numerically from the occupied and unoccupied self-consistent single-electron Kohn-Sham orbitals around E_F. In perfect spherical symmetry the energy levels $E_{n,l}$ are highly degenerate $[2(2l+1)]$ and the single-electron spectrum exhibits a well-developed electronic shell structure.[65] Moreover the radial extent of the electronic states is strongly dependent on the angular momentum quantum number l. In a real particle, numerous factors (the ionic lattice, the surface corrugation, the shape distortion, the temperature effects) remove the orbital degeneracy and lead to a strong smoothing of the density of states. In order to circumvent the problems resulting from the overestimated electronic shell structure and avoid the selection of too specific states for each size, $P(r)$ has been defined in averaging the density probability of all states in the energy range $[E_F-0.5$ eV, $E_F+0.5$ eV] for a large particle ($N=3.10^4$, i.e., $D\approx10$ nm). As for the density $n_e(r)$ the surface profile of $P(r)$ is almost size independent and a simple scaling law can be used to estimate it for each cluster size. As compared to

$n_e(r),P(r)$ extends more beyond the particle radius R_N and the Friedel oscillations are more pronounced (Fig. 12). The first feature is due to the fact that, owing to the smoothness of the surface profile of the self-consistent potential confining the electrons, the outer classical turning points for the energies $E\approx E_F$ are located in average at larger distances than those corresponding to the ground-state occupied levels ($E<E_F$). The second feature is merely due to the restricted energy-level range from which is defined $P(r)$ (the damping of the oscillations inside the particle, which stems from the dephasing of the various involved wave functions, is less pronounced).

The computed size dependence is comparable to that obtained with the first model (Fig. 13). An overestimation of the thermalization times for very small particles is however observed. In addition the predicted size effects are found weaker in this second approach, over the entire size range in spite of the larger spillout tail exhibited by the weighting function $P(r)$ [$P(r)$ is, as compared to $n_e(r)$, more localized in the surface region, Fig. 12]. This is explained by the influence of the factor $(E_F)^{-1/2}\propto n_e^{-1/3}$ entering the electron-scattering rate γ_{ee} [Eq. (10)]. In this second approach, the low surface-tail density plays a less important part in the size effects since the first multiplicative factor scales now as $n_e^{-1/2}\epsilon_b^{-1/2}$.

Though a good agreement with the experimental data is obtained, the above model based on a simple extension of the solid approach and a local description of electron-electron scattering is only a crude approach. While keeping its present form, several improvements could be introduced, for instance, in using electronic wave functions appropriate to spherical particles instead of plane waves. In particular, the momentum conservation inferred by the bulk model becomes irrelevant in spherical symmetry. The local approach is also not consistent with the delocalization of the electronic states. However, evaluation of the screening by the conduction electrons, or equivalently the determination of the nonlocal electron-gas dielectric function, is not an easy task in a finite system, owing to the translation symmetry breaking. A more adapted model introducing confinement in a more consistent way has still to be developed.

VI. CONCLUSION

The internal electron thermalization dynamics has been investigated in metal clusters using a two-color femtosecond absorption saturation technique. Experiments were performed in silver and gold nanoparticles with size ranging from 2 to 26 nm, embedded in different dielectric matrix or deposited on a substrate. In both metals the establishment of an electron temperature is shown to take place on a few hundred femtosecond time scale, comparable to the one in metal films for large particles. It is strongly accelerated for small nanoparticles ($D\leqslant10$ nm, i.e., about 3×10^4 atoms) with a 2–3 times fastening for clusters in the 2-3 nm diameter range (i.e., 250–820 atoms). The measured time-dependent signals and their probe wavelength dependences were found to be in good agreement with the calculated optical responses using numerical simulations of the time-

dependent electron distribution functions and the bulk-material band-structure models. The temporal shapes were found to be independent of the electron excitation amplitude and of the matrix and synthesis procedure of the nanoparticle samples. This permits to ascribe the observed thermalization fastening to increase of the electron-electron energy exchanges in small particles.

The size dependence of the thermalization time is in good agreement with a simple model which phenomenologically introduces increase of the Coulombic electron-electron interactions close to the surface. It relies on an extension of the bulk metal approach and on spatial average of the electron scattering rate, modeling the cluster by an ensemble of independent spherical layers. The increase of the electron-electron scattering is thus ascribed to local reduction of the Coulomb potential screening due to the spillout of the conduction electrons and to the core electrons exclusion from the surface vicinity. These surface effects were introduced in a classical approach but actually reflects the manifestation of the quantum confinement of the electronic states on the electron kinetics. Its modeling requires a full quantum description of electron-electron coupling and many-body effects in a metal cluster, starting from the spherical electron wave function. Though many theoretical works have been devoted to the description of metal cluster electronic properties, little is known about electron scattering and correlation effects. Additional theoretical works are here clearly necessary to describe the size dependence of the electron kinetics and, in particular, the transition from a bulk metal to small size clusters.

---

*Present address: Laboratoire Pierre Aigrain, Ecole Normale Supérieure, 24 rue Lhomond, 75005 Paris, France

†Present address: Physics Division, School of Technology, Aristotle University of Thessaloniki, 54124 Thessaloniki, Greece.

[1] J. Shah, *Ultrafast Spectroscopy of Semiconductors and Semiconductor Nanostructures* (Springer-Verlag, Berlin, 1996).

[2] N. Del Fatti and F. Vallée, C. R. Phys. **3**, 365 (2002), and references therein.

[3] S. Link and M.A. El-Sayed, J. Phys. Chem. B **103**, 8410 (1999), and references therein.

[4] C. Voisin, N. Del Fatti, D. Christofilos, and F. Vallée, J. Phys. Chem. B **105**, 2264 (2001).

[5] T. Tokizaki, A. Nakamura, S. Kavelo, K. Uchida, S. Omi, H. Tanji, and Y. Asahara, Appl. Phys. Lett. **65**, 941 (1994).

[6] J.Y. Bigot, J.C. Merle, O. Cregut, and A. Daunois, Phys. Rev. Lett. **75**, 4702 (1995).

[7] M. Perner, P. Bost, U. Lemmer, G. von Plessen, J. Feldmann, U. Becker, M. Mennig, M. Schmitt, and H. Schmidt, Phys. Rev. Lett. **78**, 2192 (1997).

[8] M. Nisoli, S. Stagira, S. De Silvestri, A. Stella, P. Tognini, P. Cheyssac, and R. Kofman, Phys. Rev. Lett. **78**, 3575 (1997).

[9] V. HaAae, J.Y. Bigot, B. Palpant, M. Broyer, B. Prével, and A. Pérez, J. Phys. Chem. B **75**, 3799 (1999).

[10] S. Link and M.A. El-Sayed, J. Phys. Chem. B **103**, 8410 (1999), and references therein.

[11] J.H. Hodak, A. Henglein, and G.V. Hartland, J. Chem. Phys. **111**, 8613 (1999).

[12] A. Arbouet, C. Voisin, P. Langot, D. Christofilos, N. Del Fatti, F. Vallée, J. Lermé, G. Celep, E. Cottancin, M. Gaudry, M. Pellarin, M. Broyer, M. Maillard, M.P. Pileni, and M. Treguer, Phys. Rev. Lett. **90**, 177401 (2003).

[13] N. Del Fatti, C. Flytzanis, and F. Vallée, Appl. Phys. B: Photophys. Laser Chem. **68**, 433 (1999).

[14] N. Del Fatti, F. Vallée, C. Flytzanis, Y. Hamanaka, and A. Nakamura, Chem. Phys. **251**, 215 (2000).

[15] C. Flytzanis, F. Hache, M. C. Klein, D. Ricard, and P. Roussignol, In *Progress in Optics*, edited by E. Wold, (North Holland, Amsterdam, 1991), Vol. 29, p. 321.

[16] M.J. Bloemer, J.W. Haus, and P.R. Ashley, J. Opt. Soc. Am. B **7**, 790 (1990).

[17] R. F. Haglund, G. Lupke, D. H. Osborne, H. Chen, R. H. Magruder, and R. A. Zuhr, In *Ultrafast Phenomena*, edited by T. Elsaesser, J. G. Fujimoto, D. A. Wiersma, and W. Zinth (Springer-Verlag: Berlin, 1998), Vol. 11, p. 356.

[18] C. Voisin, D. Christofilos, N. Del Fatti, F. Vallée, B. Prével, E. Cottancin, J. Lermé, M. Pellarin, and M. Broyer, Phys. Rev. Lett. **85**, 2200 (2000).

[19] For a review, see F. Vallée, C. R. Acad. Sci. Paris **2**, 1469 (2001).

[20] C.K. Sun, F. Vallée, L.H. Acioli, E.P. Ippen, and J.G. Fujimoto, Phys. Rev. B **50**, 15 337 (1994).

[21] R. Groeneveld, R. Sprik, and A. Lagendijk, Phys. Rev. B **51**, 11 433 (1995).

[22] N. Del Fatti, C. Voisin, M. Achermann, S. Tzortzakis, D. Christofilos, and F. Vallée, Phys. Rev. B **61**, 16 956 (2000).

[23] C. Voisin, D. Christofilos, N. Del Fatti, and F. Vallée, Eur. Phys. J. D **16**, 139 (2001).

[24] U. Kreibig, in *Handbook of Optical Properties*, edited by R. E. Hummel and P. Wissmann (CRC Press, New York, 1997), Vol. 2, p. 145.

[25] A. Kawabata and R. Kubo, J. Phys. Soc. Jpn. **21**, 1765 (1966).

[26] B. Lamprecht, A. Leitner, and F.R. Aussenegg, Appl. Phys. B: Lasers Opt. **68**, 419 (1999).

[27] B. Lamprecht, J.R. Krenn, A. Leitner, and F.R. Aussenegg, Phys. Rev. Lett. **83**, 4421 (1999).

[28] T. Vartanyan, M. Simon, and F. Träger, Appl. Phys. B: Laser Opt. **68**, 425 (1999).

[29] J. Bosbach, C. Hendrich, F. Stietz, T. Vartanyan, and F. Träger, Phys. Rev. Lett. **89**, 257404 (2002).

[30] N. W. Ashcroft and N. D. Mermin, *Solid State Phys.* (Holt-Saunders, Tokyo, 1981).

[31] M. Aeschlimann, M. Bauer, S. Pawlik, W. Weber, R. Burgermeister, D. Oberli, and H.C. Siegmann, Phys. Rev. Lett. **79**, 5158 (1997).

[32] P.B. Johnson and R.W. Christy, Phys. Rev. B **6**, 4370 (1972).

[33] T. Hollstein, U. Kreibig, and F. Leis, Phys. Status Solidi B **82**, 545 (1977).

[34] E. D. Palik, *Handbook of Optical Constants of Solids* (Academic Press, New York, 1985), Vols. I and II.

[35] H. Ehrenreich and H.R. Philipp, Phys. Rev. **128**, 1622 (1962).

[36] J. Lermé, B. Palpant, B. Prével, E. Cottancin, M. Pellarin, M. Treilleux, J.L. Vialle, A. Perez, and M. Broyer, Eur. Phys. J. D **4**, 95 (1998).

[37] L. Genzel, T.P. Martin, and U. Kreibig, Z. Phys. B **21**, 339 (1975).

[38] W.P. Halperin, Rev. Mod. Phys. **58**, 533 (1986).

[39] U. Kreibig, U. and M. Vollmer, *Optical Properties of Metal Clusters* (Springer, Berlin, 1995).

[40] F. Vallée, N. Del Fatti, and C. Flytzanis, in *Nanostructured Materials*, edited by V. M. Shalaev and M. Moskovits, (American Chemical Society, Washington, 1997), p. 70.

[41] J.C. Maxwell-Garnett, Philos. Trans. R. Soc. London **203**, 385 (1904); **205**, 237 (1906).

[42] D. Ricard, in *Nonlinear Optical Materials: Principles and Applications*, edited by V. Degiorgio and F. Flytzanis, (IOS Press, Amsterdam, 1995), p. 289.

[43] G. Mie, Ann. Phys. (Leipzig) **25**, 377 (1908).

[44] R. Rosei, Phys. Rev. B **10**, 474 (1974).

[45] R. Rosei, F. Antonangeli, and U.M. Grassano, Surf. Sci. **37**, 689 (1973).

[46] N. Del Fatti, R. Bouffanais, F. Vallée, and C. Flytzanis, Phys. Rev. Lett. **81**, 922 (1998).

[47] K. Uchida, S. Kaneko, S. Omi, C. Hata, H. Tanji, Y. Asahara, A.J. Ikushima, T. Tokisaki, and A. Nakamura, J. Opt. Soc. Am. B **11**, 1236 (1994).

[48] B. Palpant, B. Prével, J. Lermé, E. Cottancin, M. Pellarin, M. Treilleux, A. Perez, J.L. Vialle, and M. Broyer, Phys. Rev. B **57**, 1963 (1998).

[49] A. Taleb, C. Petit, and M.P. Pileni, Chem. Mater. **9**, 950 (1997).

[50] J.W. Slot and H.J. Geuze, Eur. J. Cell Biol. **38**, 87 (1985).

[51] R. Rosei, C.H. Culp, and J.H. Weaver, Phys. Rev. B **10**, 484 (1974).

[52] H. Inouye, K. Tanaka, I. Tanahashi, and K. Hirao, Phys. Rev. B **57**, 11 334 (1998).

[53] Y. Hamanaka, J. Kuwabata, I. Tanahashi, S. Omi, and A. Nakamura, Phys. Rev. B **63**, 104302 (2001).

[54] N. Del Fatti and F. Vallée, Appl. Phys. B: Lasers Opt. **73**, 383 (2001).

[55] G.V. Hartland, J.H. Hodak, and I. Martini, Phys. Rev. Lett. **82**, 3188 (1999).

[56] S. Link, C. Burda, Z.L. Wang, and M.A. El-Sayed, J. Chem. Phys. **111**, 1255 (1999).

[57] D. Pines and P. Nozières, *The Theory of Quantum Liquids* (Benjamin, New York, 1966).

[58] D.W. Snoke and J.P. Wolfe, Phys. Rev. B **39**, 4030 (1989).

[59] D.W. Snoke, W.W. Rhle, Y.C. Lu, and E. Bauser, Phys. Rev. B **45**, 10 979 (1992).

[60] S. Ogawa, H. Nagano, and H. Petek, Phys. Rev. B **55**, 10 869 (1997).

[61] V.A. Gasparov and R. Huguenin, Adv. Phys. **42**, 393 (1993).

[62] W. Ekardt, Phys. Rev. B **29**, 1558 (1984).

[63] V.V. Kresin, Phys. Rep. **220**, 1 (1992).

[64] W.A. de Heer, Rev. Mod. Phys. **65**, 611 (1993).

[65] M. Brack, Rev. Mod. Phys. **65**, 677 (1993).

[66] C. Bréchignac, P. Cahuzac, J. Leygnier, and A. Sarfati, Phys. Rev. Lett. **70**, 2036 (1993).

[67] A. Liebsch, Phys. Rev. B **48**, 11 317 (1993).

[68] V.V. Kresin, Phys. Rev. B **51**, 1844 (1995).

[69] J. Tiggesbumker, L. Kller, K.H. Meiwes-Broer, and A. Liebsch, Phys. Rev. A **48**, R1749 (1993).

[70] J. Lermé, B. Palpant, B. Prével, M. Pellarin, M. Treilleux, J.L. Vialle, A. Perez, and M. Broyer, Phys. Rev. Lett. **80**, 5105 (1998).

[71] N. Nilius, N. Ernst, and H.-J. Freund, Phys. Rev. Lett. **84**, 3994 (2000).

[72] J. Kliewer, R. Berndt, E.V. Chulkov, V.M. Silkin, P.M. Echenique, and S. Crampin, Science **288**, 1399 (2000).

[73] L. Bürgi, O. Jeandupeux, H. Brune, and K. Kern, Phys. Rev. Lett. **82**, 4516 (1999).